

## Research Article

# Seismic Behavior and Finite Element Analysis of Reinforced Concrete Short Columns Impacted by Oblique Earthquakes

Chunyang Liu <sup>1,2</sup>, Guixin Yu,<sup>1</sup> Xisen Fan,<sup>1,2</sup> Changqun Guo,<sup>1</sup> and Fei Li<sup>1</sup>

<sup>1</sup>Department of Civil Engineering, Shandong Jianzhu University, Jinan 250101, China

<sup>2</sup>Key Laboratory of Building Structural Retrofitting and Underground Space Engineering (Shandong Jianzhu University), Ministry of Education, Jinan 250101, China

Correspondence should be addressed to Chunyang Liu; liucy2011@sdjzu.edu.cn

Received 19 January 2020; Revised 24 June 2020; Accepted 12 September 2020; Published 30 September 2020

Academic Editor: Antonio Formisano

Copyright © 2020 Chunyang Liu et al. This is an open access article distributed under the Creative Commons Attribution License, which permits unrestricted use, distribution, and reproduction in any medium, provided the original work is properly cited.

This study evaluates the seismic behavior of reinforced concrete (RC) short columns with a high axial compression ratio under oblique earthquake conditions. The studied parameters include the loading angle, axial compression ratio, the high-strength stirrups with small spacing, and the carbon-fiber-reinforced polymer (CFRP) wrapped column end or outer steel plate mesh at the end of the column. Low-cycle repeated loading tests were used to analyze the specimens' seismic performance indices of hysteretic behavior, strength, stiffness, deformation capacity, and energy dissipation capacity. Results suggest that the OpenSees finite element program can sufficiently simulate the nonlinear response of the specimen. Oblique loading led to the increase of damage to the specimens and the deterioration of stiffness of the specimens, which was especially seen with the increase of the axial compression ratio. Accordingly, arranging high-strength stirrups with small spacing and the column end outer steel plate mesh both transform the failure mode from shear failure to bending shear failure. Additionally, wrapping the CFRP at the end of columns improves their strength but does not improve their deformation capacity. The demonstrated success of these strategies in improving the seismic performance of RC short columns under diagonal loads with high axial compression ratios can inform practical engineering applications.

## 1. Introduction

Seismic damage investigations have shown that reinforced concrete (RC) short columns are prone to shear damage under strong ground motions, which can cause severe damage or even collapse of the RC frame structure [1,2]. One of the reasons for this tendency for severe earthquake damage is that the direction of strong ground motion on the RC short columns is arbitrary [3,4]. RC short columns are subjected to horizontal earthquakes transmitted according to the two horizontal adjacent components effect; this effect causes the component, i.e., the columns, to withstand greater forces than a single horizontal direction and thus typically causes greater damage. Researchers have examined the performance of RC short columns under a variety of seismic conditions. For example, Woodward and Jirsa [5] and Maruyama et al. [6] studied the effect of load direction on the

shear performance and stiffness of RC short columns; they showed that the cumulative damage caused by the loading of the specimens in different directions reduces the stiffness of the concrete column but has little effect on the shear capacity of the specimens. Rodrigues et al. [7] studied the seismic performance of reinforced concrete columns under bidirectional cyclic loading. The results showed that the bidirectional cyclic loading led to a decrease in the stiffness and strength of the column and affected the ductility and energy dissipation capacity of the column. When RC short columns are used in high-rise buildings and super high-rise buildings, they experience high vertical loads, resulting in a generally high axial compression ratio when the column section size is constant. Previous research demonstrated that when an earthquake occurred, the RC column was affected by both the axial force and the vertical ground motion [8,9]. The strong vertical ground motion increased the axial force of

the RC short column, resulting in the axial compression ratio of the short column approaching or exceeding the design limits and contributing to the component's being severely damaged in the earthquake. These results indicate that the seismic performance of RC short columns in the oblique or nonspindle direction under high axial compression ratio needs further study. Zhou and Liu [10] examined the behavior of RC short columns with axial compression ratios ranging from 0.35 to 0.55. Ma et al. [11] examined the behavior of RC short columns with axial compression ratios ranging from 0.3 to 0.9. However, the seismic performance of these RC short columns under high axial pressures during oblique earthquake action is currently not adequately characterized.

Researchers have conducted research on various approaches to effectively improve the problem of shear failure of RC short columns under strong ground motion. Considering the characteristics of high-strength steel bars with high yield strength and good toughness, the application of such research to concrete structures is conducive to improving the seismic performance of various structures with RC short columns. Sokoli and Ghannoum [12] studied the applicability of high-strength longitudinal reinforcements in RC columns; the results showed that high-strength longitudinal reinforcement could achieve shear force transmission mechanisms that enable RC columns to meet seismic requirements. Ding et al. [13] studied the seismic performance of high-strength stirrup restraining high-strength concrete short columns; results showed that the restraining effect of high-strength stirrup on the concrete improved the strength and seismic performance of the specimen. Further, Shin et al. [14] also proved that high-strength stirrups with good restraint can provide effective restraint for longitudinal reinforcement and improve the strength, ductility, and energy consumption of the column. While the addition of high-strength steel stirrups to RC short columns can improve characteristics of these components, researchers have also considered reinforcement with carbon-fiber-reinforced polymer (CFRP). For example, Shehata et al. [15] studied the ductile properties of CFRP-wrapped RC short columns; results show that the ultimate deformation of the specimen depends on the lateral restraint strength. Colomb et al. [16] studied the effect of CFRP on the failure mode of RC short columns; results showed that the reinforcement mode of CFRP changed the failure mode of RC short columns, such that the specimens changed from shear brittle failure to ductile bending shear failure. Galal et al. [17] conducted research on the seismic performance of RC short columns restrained by CFRP; results showed that the RC short columns restrained by CFRP can effectively improve the shear capacity and energy dissipation capacity of the specimen. As an alternative to CFRP, researchers also consider using steel plate mesh to strengthen reinforced concrete columns. For example, Morshed and Kazemi [18] studied the seismic performance of concrete short columns confined by a steel mesh; results showed that the steel plate mesh constraints significantly improved the shear resistance and deformation ability of RC columns. Li et al. [19] subjected high-strength RC columns containing steel plate mesh restraints to low-

cycle repeated loading tests; results showed that the hysteresis curve of the outsourced expanded steel mesh constrained specimen was full, the strength and ductility of the specimen significantly improved, and the stiffness degradation slowed. The collective results of research on the effects of arranging dense high-strength stirrups, CFRP, and steel plate mesh on the performance of RC short columns show that these reinforcements improve the seismic performance of RC short columns in the main axis direction. Therefore, under oblique earthquake action, these reinforcements have demonstrated a significant ability to improve the seismic performance of RC short columns with high axial compression ratios.

Here, six short concrete columns with high-strength longitudinal reinforcement were designed and subjected to repeated low-cycle loading tests. The effects of the loading angle, axial compression ratio, dense high-strength stirrups, column-end wound carbon fiber cloth, and column-end coated steel mesh on the hysteretic characteristics, strength, stiffness, deformation capacity, and energy dissipation capacity of the test pieces were analyzed. Test results were then compared to those obtained by OpenSees simulation. This study is intended to provide a reference for improving the seismic performance of RC short columns under diagonal loads with high axial compression ratios.

## 2. Experimental Program

*2.1. Specimen Design.* This study used six RC short column specimens (Table 1), referred to as SC-1 through SC-6. SC-1 was a comparative specimen with a  $0^\circ$  horizontal loading. SC-2 through SC-6 were loaded at a  $45^\circ$  oblique loading. SC-4 included dense high-strength stirrups, that is, a specimen configured with small spacing high-strength stirrup, whereas SC-5 and SC-6 were partially strengthened with either column-end winding CFRP (A; Table 1) or column-end outer steel mesh (B; Table 1). All specimens had  $300\text{ mm} \times 300\text{ mm}$  cross sections and C40 concrete design strength with a 20 mm thick protective layer. The longitudinal reinforcement in the column was made of 12 HTRB630 high-strength steel bars with a 16 mm diameter. These bars were evenly distributed along the section to achieve a reinforcement ratio of 2.68%. In the experiments, the stirrup grade was varied as either HRB400 or HTRB630, both of which had diameters of 8 mm (Table 1). All stirrups were in the form of well-typed composite stirrups with varied stirrup spacing and volume stirrup ratios (Table 1). The distance between the horizontal loading point of the specimen and the bottom of the column was 600 mm, and the shear span ratio was 2. The dimensions of the specimen and the reinforcement of the section were varied among specimen types (Figure 1). Considering the influence of different loading directions on the seismic performance of the specimen, two typical directions of load loading,  $0^\circ$  and  $45^\circ$ , were selected for this test. Considering that the axial compression ratio of RC short columns in actual engineering meets or even exceeds the design upper limit, the design axial compression ratio ( $n$ ) of this test was selected to be 0.8 and 1.0. Considering that the common stirrups under high

TABLE 1: Design parameters of specimens.

Specimen	$\alpha$ (°)	$n$	Strengthening measures	Stirrup grade	Stirrup		$\rho_v$ (%)
					Diameter	@spacing (mm)	
SC-1	0	0.8	—	HRB400	8@80	8@80	1.90
SC-2	45	0.8	—	HRB400	8@80	8@80	1.90
SC-3	45	1.0	—	HRB400	8@80	8@80	1.90
SC-4	45	1.0	—	HTRB630	8@50	8@50	3.05
SC-5	45	1.0	A	HTRB630	8@50	8@50	3.05
SC-6	45	1.0	B	HTRB630	8@50	8@50	3.05

Note. SC = short column;  $\alpha$  = loading direction;  $n = N/f_c b h$ , where  $N$  is the design value of axial pressure,  $f_c$  is the design value of concrete strength,  $b$  is the column section width, and  $h$  is the column section height;  $\rho_v$  is the rebar ratio.

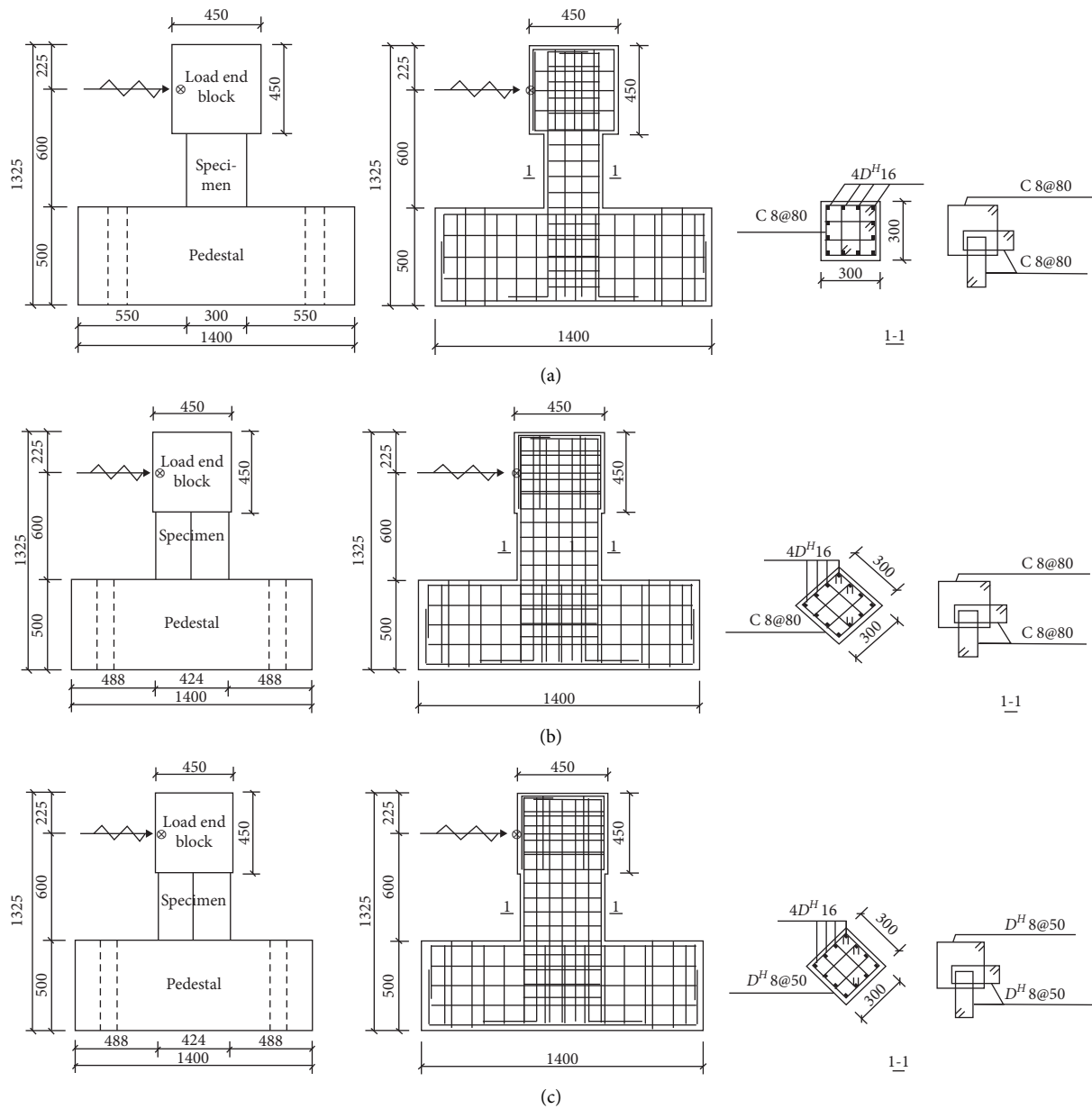


FIGURE 1: Schematics of prepared specimens, i.e., short column-1 (SC-1) through SC-6, including arrangement of reinforcing bars:  $D^H$  = HTRB630 steel bar and C = HRB400 steel bar;  $\otimes$  = horizontal load loading point. (a) SC-1. (b) SC-2, SC-3 (c) SC-4, SC-5, and SC-6.

axial compression ratio have the challenge of premature yielding and short-column brittle failure, HRB400 and HTRB630 rebars were selected for this test. The mechanical properties of the concrete used in this study (outlined in Table 2) were held constant, whereas the mechanical properties of the three types of steel bars (outlined in Table 3) and the two types of reinforcing materials (outlined in Table 4) were previously characterized.

Production of the specimens SC-1 through SC-4 involved first ligating the longitudinal reinforcements and the stirrups to form a steel cage. Formwork and concrete pouring were then completed. To facilitate test loading, obliquely loaded column sections were placed at a 45° to the base. Specimen SC-5 involved wrapping the end of the column with CFRP, which had a single layer thickness of 0.11 mm and a total of three layers, totaling 200 mm in total height. At the time of construction, the steel bars were first tied to form a steel cage; the concrete was then poured and cured. To avoid tearing of the CFRP, the chamfer radius of the corner was 25 mm. This method was used to improve the restraint effect of the column-end concrete as well as to improve the seismic performance of the specimen.

SC-6 involved reinforcement with a column-end outer steel plate mesh. The steel plate mesh adopted a round hole steel plate mesh with a wrapping height of 300 mm, a thickness of 3 mm, a circular hole diameter of 5 mm, and a hole pitch of 5 mm, which was processed into a square pattern (Figure 2(a)). First, the U-shaped snap fastener was placed on the longitudinal bar and fixed at the joint of the longitudinal reinforcement and the stirrup passing through the screw and tightening the nut (Figures 2(b) and 2(c)). Then, the steel plate mesh was placed on the outer side of the steel skeleton to make the inner surface of the steel plate mesh tightly attached to the outer side of the U-shaped snap fastener (Figure 2(d)). To ensure that the steel plate mesh did not participate in the force of the column end, a 5 mm gap was left between the end portion and the column base. After placement, the steel plate mesh was fixed with local winding wires. After construction of the steel skeleton, the concrete was poured, resulting in the surface of the column being flush with the surface of the steel plate mesh. This method was used to improve the restraining effect on the column-end concrete and to improve the seismic performance of the specimen.

**2.2. Load Method.** Vertical loads were applied in the axial direction, using a 200 ton vertical actuator, and held constant at the designated axial compression ratios. The actuator used was made in China. The horizontal load tests were conducted by adopting the low-cycle repeated loading mode. The tests were performed by conducting displacement-controlled loading, with the displacement cycle loaded twice per stage until the load dropped to either 85% of the peak load or to the point at which the specimen was not suitable for carrying the load (Figure 3). It was assumed that positive force and displacement were produced by the thrust of the actuator and that negative force and displacement were produced by the pull force caused by the actuator. The

TABLE 2: Mechanical properties of the concrete.

Concrete grade	$f_{cuk}$ (MPa)	$f_{ck}$ (MPa)	$E_c$ (MPa)
C40	60.4	45.3	$3.60 \times 10^4$

Note.  $f_{cuk}$  is the compressive strength of concrete cubes;  $f_{ck}$  is the compressive strength of concrete prism;  $E_c$  is the elastic modulus of concrete.

TABLE 3: Mechanical properties of reinforced bars.

Steel bar type	Diameter (mm)	$f_y$ (MPa)	$f_u$ (MPa)	$\delta$ (%)	$E_s$ (MPa)
HRB400	8	488	640	26.25	$2.02 \times 10^5$
HTRB630	8	601	855	23.8	$2.29 \times 10^5$
HTRB630	16	668	845	23.0	$2.45 \times 10^5$

Note.  $f_y$  is the rebar yield strength;  $f_u$  is the rebar ultimate strength;  $\delta$  is the rebar elongation after breaking; and  $E_s$  is the rebar modulus of elasticity.

TABLE 4: Mechanical properties of strengthening material.

Material type	Thickness (mm)	$f_y$ (MPa)	$f_u$ (MPa)	$E_s$ (MPa)
Steel plate mesh	3	208	313	$1.68 \times 10^5$
CFRP	0.167	–	3471	$2.31 \times 10^5$

loading displacement of the column-end load point was implemented by an MTS 100 ton horizontal actuator. This actuator was made in the United States and incorporates an associated data acquisition system that collects the load and displacement data (Figure 4). Collected data were used to generate a hysteresis curve. Cracks on the specimen were visually observed and manually mapped.

### 3. Experimental Results and Analysis

**3.1. Failure Modes.** Application of loads resulted in variable states of damage to all specimens tested in this study based on visual observations. The definition of the observation surface of each specimen is shown in Figure 5. The final failure mode of each specimen is shown in Figure 6.

For specimen SC-1, small horizontal cracks appeared within a range of 300 mm from the column bottom when the horizontal displacement of the column top was loaded to 1.5 mm; as the loading continued, the number of cracks increased. At 18.2 mm, the concrete at the bottom corner of the column fell off, and some longitudinal reinforcements and stirrups were exposed. When specimen was broken, the longitudinal reinforcements in the southwest corner broke. Accordingly, specimen SC-1 has obvious shear failure characteristics (Figure 6(a)). Regarding specimen SC-2, at 1.5 mm, small horizontal cracks appeared within a range of 150 mm from the column bottom; as the loading continued, horizontal cracks developed into oblique cracks and the number of cracks increased. At 18.2 mm, the concrete in the corner of the column fell off, and some longitudinal reinforcements and stirrups were exposed. When the specimen was broken, the corner concrete severely fell off, and the longitudinal reinforcement in the corners in the east and west directions broke. Accordingly, specimen SC-2 has obvious shear failure characteristics (Figure 6(b)). Regarding

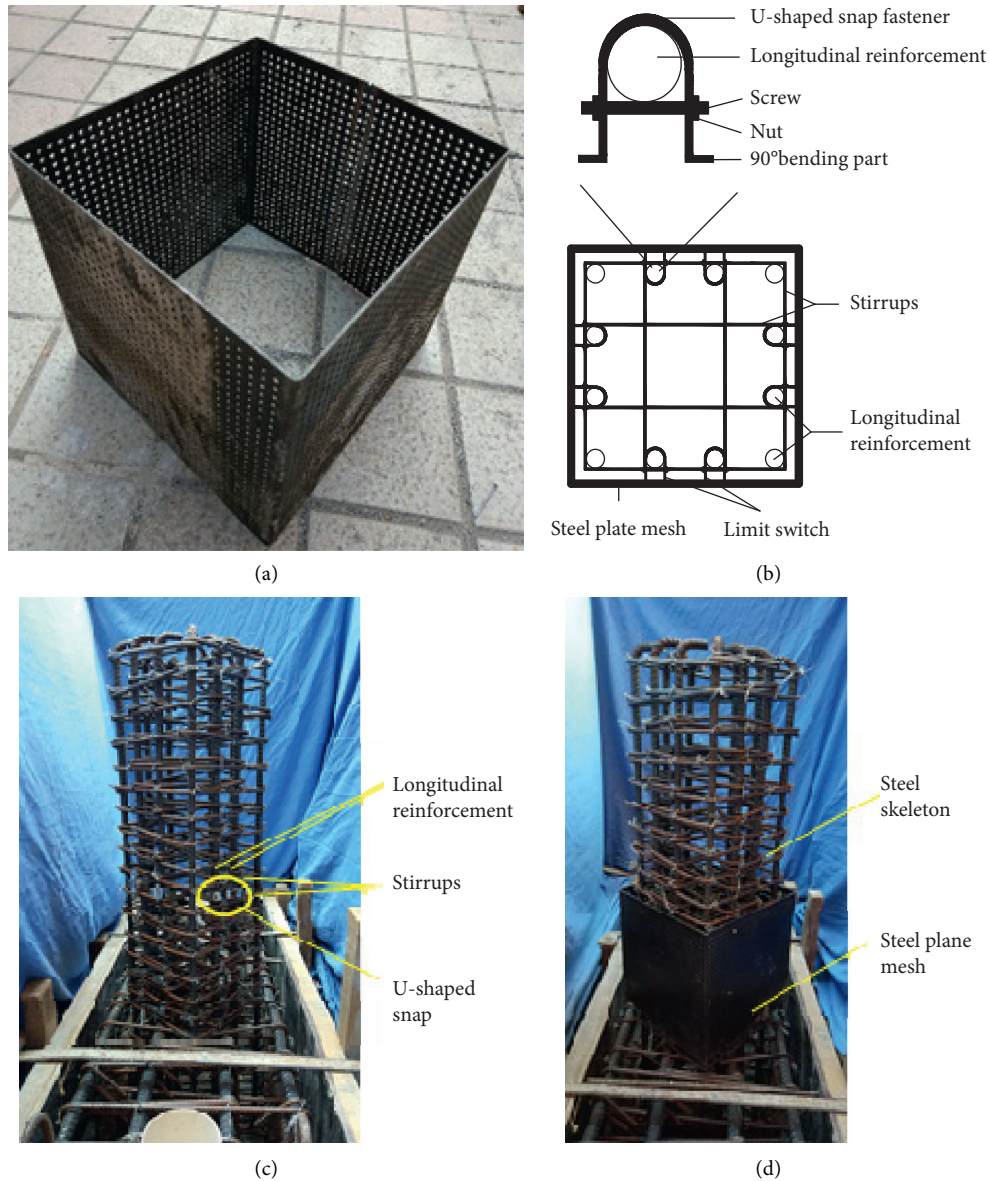


FIGURE 2: Details of steel skeleton production. (a) Steel plate mesh, (b) limit device floor plan, (c) steel skeleton with U-shaped snap fastener, and (d) steel skeleton with steel plate mesh.

specimen SC-3, at 1.5 mm, small horizontal cracks appeared within a range of 200 mm from the column’s bottom; when the loading continued, the number of cracks increased and penetration cracks appeared. At 15 mm, the concrete fell off, and some longitudinal reinforcements and stirrups were exposed. When the specimen was broken, the concrete in the core area had been crushed, and some longitudinal reinforcements were broken. Accordingly, specimen SC-3 has obvious shear failure characteristics (Figure 6(c)).

Regarding specimen SC-4, at 1.5 mm, small horizontal cracks appeared within a range of 150 mm from the column bottom; as the loading continued, the number of cracks increased. At 32 mm, the northwest concrete began to fall off and the longitudinal tendons broke. When the specimen was damaged, the concrete at the bottom corner of the column in the east and west directions was crushed, and the

longitudinal tendons broke. Accordingly, the bending and shear failure characteristics of specimen SC-4 can be seen (Figure 6(d)). Regarding specimen SC-5, at 1.5 mm, cracks appeared on the edge of the CFRP; when the loading continued, the number of cracks increased and penetrating cracks appeared. At 18.2 mm, the concrete started to fall off and the carbon fiber cloth cracked. When specimen was broken, the concrete at the bottom corner of the column in the east and west directions was crushed (Figure 6(e)). After the test, the carbon fiber cloth was peeled off; it was found that the column-angle concrete had been significantly broken diagonally, and the longitudinal tendons and stirrups had become exposed. Accordingly, specimen SC-5 has shear failure characteristics (Figure 6(f)). Regarding specimen SC-6, at 3 mm, cracks appeared on the edge of the steel plate mesh; as loading continued, the number of cracks increased.

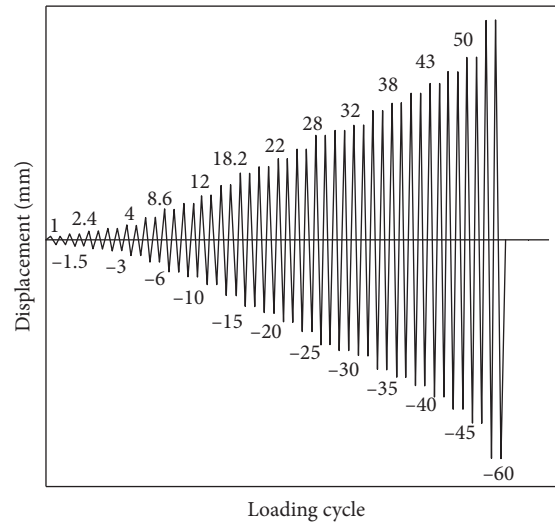


FIGURE 3: Loading protocol. The tests performed via displacement-controlled loading.

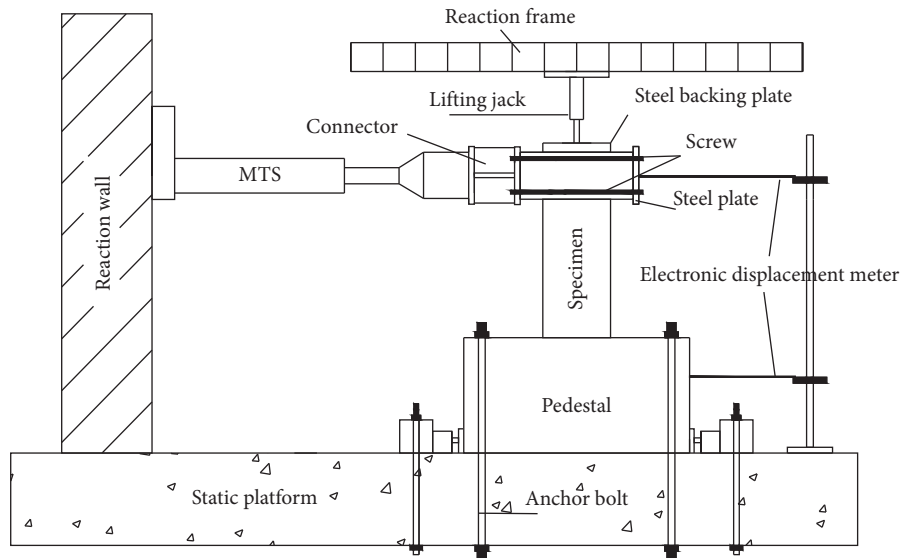


FIGURE 4: Experimental test set-up. MTS actuator with data acquisition system collects load and displacement data.

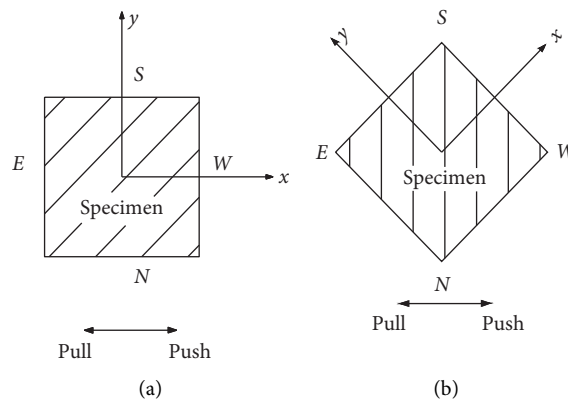


FIGURE 5: Definition of specimen observation surface. (a) Spindle loading; (b) 45° loading.

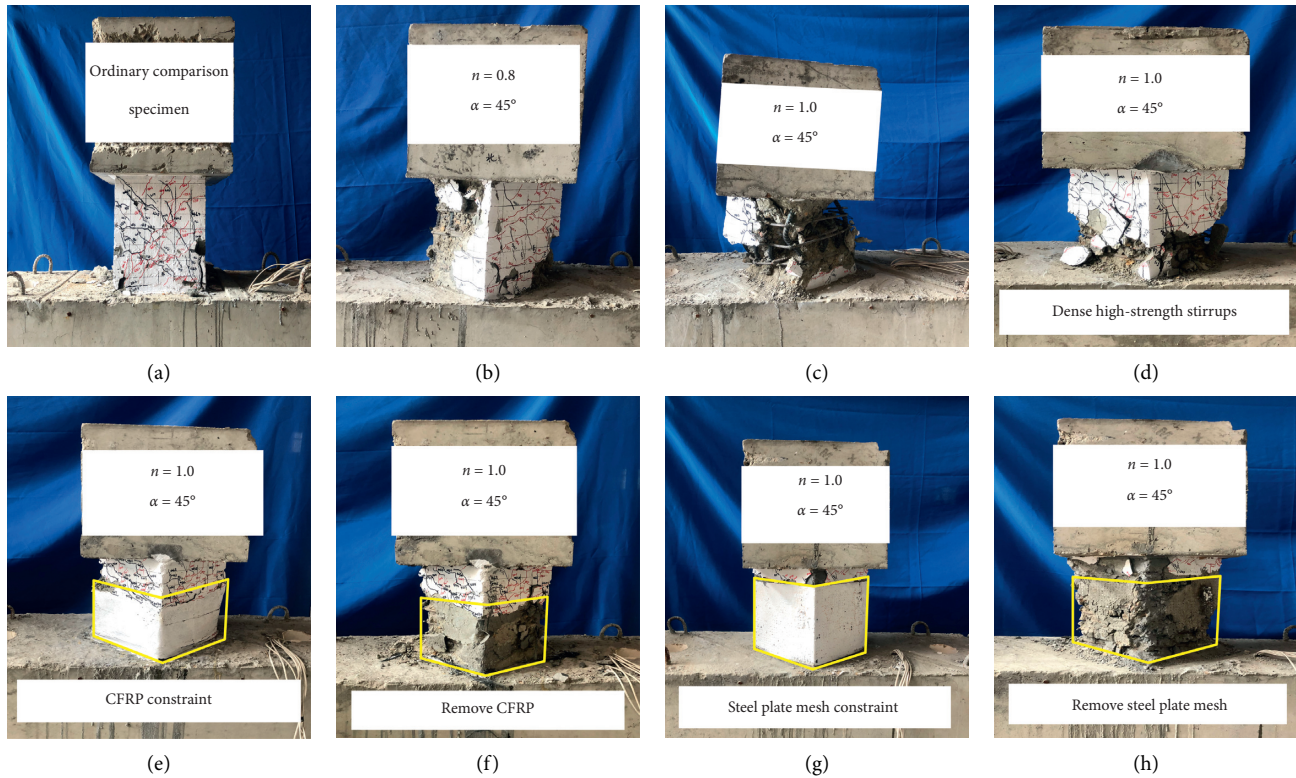


FIGURE 6: Visual observations of the ultimate failure modes of short column (SC) specimens. (a) SC-1, (b) SC-2, (c) SC-3, (d) SC-4, (e) SC-5, (f) SC-5 after removal of CFRP, (g) SC-6, and (h) SC-6 after removal of steel plate mesh.

At 40 mm, the longitudinal reinforcement was broken. When the specimen was broken, the steel plate mesh at the bottom of the column was convex (Figure 6(g)). After the test, the steel plate mesh was peeled off; it was found that the concrete at the bottom of the column was broken, and the longitudinal steel bars were convex and partially broken. Accordingly, the bending and shear failure characteristics of specimen SC-6 can be seen (Figure 6(h)).

Overall, compared with the horizontally loaded test specimens, the concrete at the corners of the diagonally loaded test specimens fell off severely, which reduced the workability of the test specimens. In particular, the increase in the axial pressure ratio makes this damage more serious. Compared to the unreinforced test specimens, high-strength stirrups with small spacing, column-end wrapped CFRP, and column-end outer steel plate mesh enhanced the restraint effect on concrete, limited concrete falling off, and improved the seismic performance of the specimens under oblique loads.

**3.2. Hysteresis Curves.** The load-displacement hysteresis curves of each specimen demonstrate the performance of each specimen during the duration of the tests (Figure 7).  $P$  is the measured horizontal load;  $\Delta$  is the measured horizontal displacement of the loading point. As can be seen from Figure 7, compared to specimen SC-1, specimen SC-2 undergoes accelerated strength degradation at a later stage of loading, and the residual deformation is larger. This could be attributed to the oblique loading that leads to the corner

concrete of the specimen being subjected to loads in two directions, resulting in serious damage to the corner concrete (Figures 7(a) and 7(b)). In contrast to specimen SC-2, specimen SC-3 has a significantly lower load at the later stage of loading; this is due to the severe fall of the concrete at the later stage of loading (Figures 7(b) and 7(c)). There were two significant drops in the hysteresis curves of SC-4 and SC-6, likely due to the fracture of the high-strength longitudinal bars, which led to a significant decline in the strength of these specimens (Figures 7(d) and 7(f)). However, the high-strength stirrups with small spacing included in these treatments provided a strong constraint effect for high-strength longitudinal bars that enabled the specimens to retain a strong strength. Compared to the hysteresis curve of specimen SC-4, that of specimen SC-5 is less full. This is because the CFRP is prone to tear and damage at the column angle under a high axial pressure ratio (Figures 7(d) and 7(e)), which causes the strength of the specimen to drop sharply. In contrast to specimen SC-4, the load of specimen SC-6 decreases slowly at the later stage of loading, and the hysteresis curve was relatively plump (Figures 7(d) and 7(f)). This is because the steel plate net at the end of the column can effectively slow the fall of concrete and exert a stronger energy consumption.

**3.3. Skeleton Curves.** In the hysteretic curve under the condition of low-cycle reciprocating loading, the outer winding line of the peak loading point of each stage is called a skeleton curve, which characterizes the characteristics of

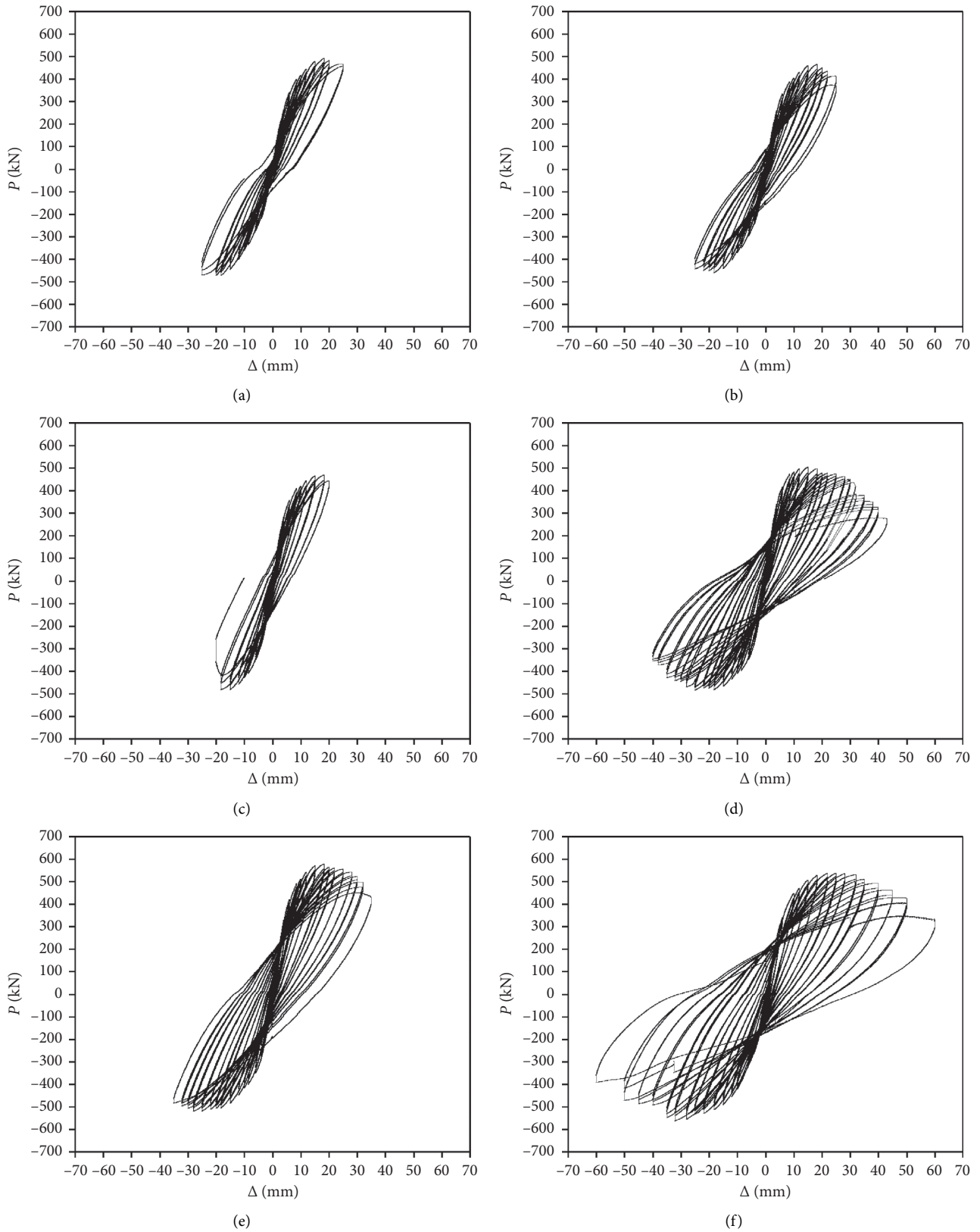


FIGURE 7: Hysteretic curves of short column (SC) specimens 1–6. (a) SC-1, (b) SC-2, (c) SC-3, (d) SC-4, (e) SC-5, and (f) SC-6.

stress and deformation during the loading of the specimen. The skeleton curve of each specimen is shown in Figure 8. As can be seen from the figure, the development of the skeleton

curves of each specimen can be roughly divided into three stages. (1) In the elastic stage, the load changes linearly with the displacement, the specimen has yet to crack, and no

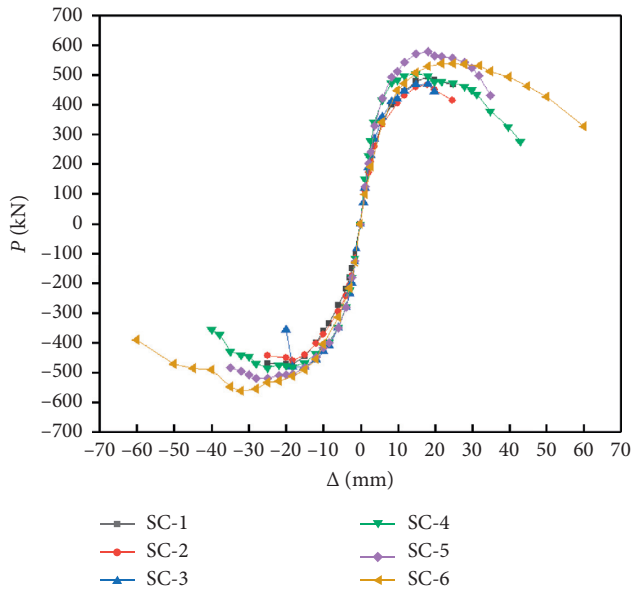


FIGURE 8: Skeleton curves of specimens. Skeleton curves represent the outer winding line of the peak loading point of each stage.

residual deformation is observed. (2) During the development stage of a multicrack, many cracks appear in the specimen. When residual deformation begins to appear, multiple tiny cracks appear on the surface of the specimen, and the horizontal load of the specimen slowly increases. With the accumulation of damage, the specimen reaches the peak load. (3) In the load drop stage, for specimens SC-1, SC-2, and SC-3, the skeleton curve decreases significantly in the later stage of loading. This is because the ordinary stirrups with large spacing cannot provide effective lateral restraints for the specimens under a high axial compression ratio, thus making the strength of the specimens drop dramatically. Compared to specimen SC-3, the skeleton curves of specimens SC-4, SC-5, and SC-6 decrease slowly and show good deformation ability. In particular, the deformation capacity of specimens SC-4 and SC-6, after the peak point, significantly improves; this is conducive to improving the seismic energy dissipation capability of specimens.

**3.4. Bearing Capacity and Ductility.** Each sample was characterized by the yield load point, the peak load point, and the failure load point within a load-displacement curve. As shown in Figure 9, the yield point D was determined by the equivalent elastic-plastic energy method, that is, where the area  $S_{OAB} = S_{BCD}$ , and the ultimate load was simply defined as 85% of the peak load. [20] Because the strength of SC-1, SC-2, and SC-3 declined rapidly after reaching the peak load and the ultimate load did not reach 85% of the peak load, the failure displacements of these were taken as the ultimate displacement. Here, the ultimate displacement angle ( $\theta_u$ ) was used to characterize the deformation ability of the specimen and was calculated as  $\theta_u = \Delta_u/l_0$ , where  $l_0$  is the column's height. For each specimen, the characteristic load and displacement calculation results are shown in Table 5.

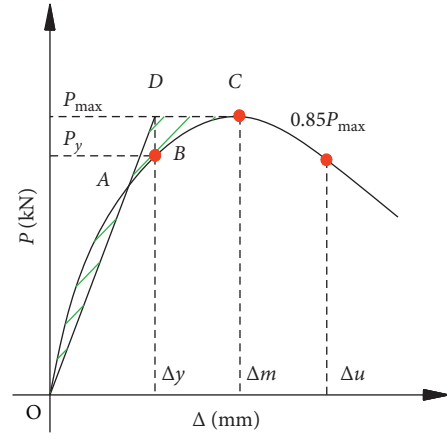


FIGURE 9: Calculation of characteristic points for each specimen.  $P_y$  is the yield load;  $P_{max}$  is the peak load.

The relative value is the ratio of the average of the positive and negative corresponding coefficients of SC-2 through SC-6 and the average of the positive and negative corresponding coefficients of SC-1.

As can be seen in Table 5, compared to specimen SC-1, the yield load, peak load, and ultimate load of specimen SC-2 are reduced, and the ultimate displacement angle is unchanged. This is because the concrete in the corner of the test specimen is severely damaged under the diagonal horizontal loading, making the strength of the specimen decrease; however, this has no effect on the deformation ability of the specimen. A comparison of SC-2 and SC-3 reveals that, under the oblique load, as the axial pressure ratio increases, the strength of the specimen increases, but the deformation capacity decreases. In contrast to specimen SC-4, the yield load, peak load, and ultimate load of SC-5 improved, whereas the ultimate displacement angle decreased by 1%. This result indicates that although the strength of the specimen under high axial pressure ratio improved, the deformation capacity of the specimen under high axial pressure ratio did not improve. Compared to specimen SC-4, the yield load, peak load, and ultimate load of specimen SC-6 improved, and the ultimate displacement angle increased by 52%. This result was likely due to the column-end outer steel plate mesh providing a strong restraining effect on the column-end concrete, which then increased the specimen's strength, deformation capacity, and seismic performance.

In comparison to SC-3, the yield load, peak load, and ultimate load of SC-4, SC-5, and SC-6 were all greatly improved, as were the ultimate displacement angles. This indicates that the high-strength stirrups with small spacing, column-end wound CFRP, and column-end outer steel plate mesh may improve the strength and the deformation ability of the RC columns; therefore, this should be considered when accounting for seismic loads in RC columns.

**3.5. Stiffness Degradation.** Stiffness degradation of a specimen under cyclic loading is usually attributable to the accumulation of specimen damage, which has great influence

TABLE 5: Experimentally derived characteristic loads and displacements for specimens SC-1 through SC-6.

Specimen	Loading direction	$P_y$ (kN)	$\Delta_y$ (mm)	$P_m$ (kN)	$\Delta_m$ (mm)	$P_u$ (kN)	$\Delta_u$ (mm)	$\theta_u$ (%)	Relative value
SC-1	+	416.50	9.86	492.50	18.20	467.94	25.00	4.17	1
	-	400.45	12.05	472.86	18.19	469.73	25.00	4.17	
SC-2	+	394.70	9.38	466.00	18.17	413.63	25.00	4.17	1
	-	381.88	10.66	459.85	18.20	443.23	25.00	4.17	
SC-3	+	408.20	8.50	470.05	18.20	443.97	20.00	3.33	0.80
	-	410.37	8.68	481.92	15.00	409.63	20.00	3.33	
SC-4	+	437.73	6.96	504.93	15.00	429.19	31.84	5.31	1.35
	-	408.28	9.72	483.11	25.00	410.64	35.95	5.99	
SC-5	+	501.21	9.17	578.02	18.20	491.32	32.23	7.61	1.34
	-	434.56	11.13	519.65	28.00	482.94	35.00	7.98	
SC-6	+	465.87	11.51	538.13	24.99	457.41	45.63	5.37	1.87
	-	483.57	14.43	561.64	32.00	477.39	47.90	5.83	

Note.  $P_y$  is the yield load,  $\Delta_y$  is the yield displacement,  $P_m$  is the peak load,  $\Delta_m$  is the peak displacement,  $P_u$  is the ultimate load,  $\Delta_u$  is the ultimate displacement, and  $\theta_u$  is the deformation ability.

on the seismic performance of the specimens. Here, the secant stiffness ( $K_i$ ) was used to represent the stiffness degradation of the specimens. The secant stiffness  $K_i$  was calculated as

$$K_i = \frac{|P_i^+| + |P_i^-|}{|\Delta_i^+| + |\Delta_i^-|}, \quad (1)$$

where  $P_i^+$  and  $P_i^-$  are the  $i$ -th positive and reverse peak loads, respectively, and  $\Delta_i^+$  and  $\Delta_i^-$  are the  $i$ -th positive and reverse peak displacements.

The stiffness degradation curve of each test piece is shown in Figure 10. As loading displacement increased, the stiffness of each specimen gradually decreased. The stiffness degraded rapidly in the early stage and slowly in the later stage. This could be due to the continuous cracking of concrete in the early stage of loading, whereas no new cracks were generated in the late loading stages; thus, when the cumulative damage of the specimen reached a certain degree, the slope of the stiffness degradation curve of the specimen decreased. Compared to specimen SC-1, the stiffness of specimen SC-2 degraded faster. This is because the oblique horizontal loading caused damage in the corner of the specimen, affecting each other. In contrast to specimen SC-2, the stiffness of specimen SC-3 decreased sharply in the later stage of loading. This is due to the higher axial compression ratio of the specimen, which caused the concrete to fall severely, the stirrups to protrude, and the longitudinal bars to yield. The stiffness degradation curves of SC-4, SC-5, and SC-6 had a slower downward trend and a longer curve extension compared to those of SC-3. This indicates that the high-strength stirrups with small spacing, the column-end wound CFRP, and the column-end outer steel plate mesh may have alleviated the damage degree of the specimen and thus slowed the degradation stiffness degradation of these specimens.

**3.6. Energy Dissipation.** The energy dissipation capacity of specimens under earthquake action is an important index for evaluating their seismic performance. Here, the equivalent viscous damping coefficient ( $h_e$ ) and cumulative energy

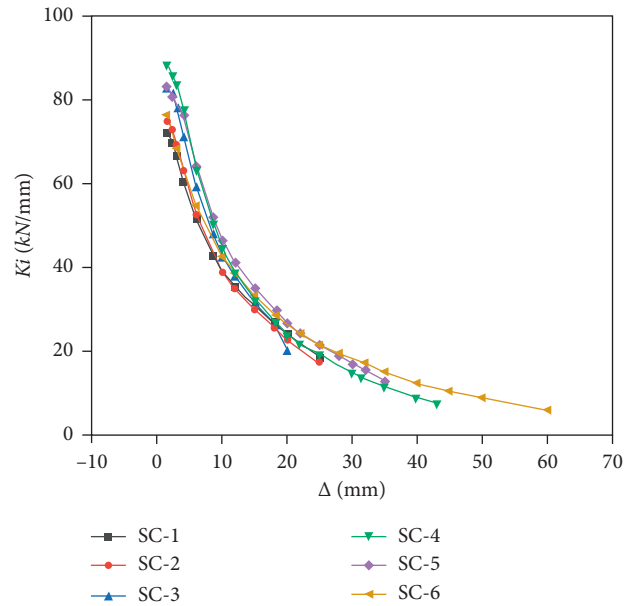


FIGURE 10: Stiffness degradation curves of specimens. Stiffness degradation of the specimens is represented by secant stiffness  $K_i$ .

consumption ( $E_p$ ) were used to characterize the energy dissipation performance of the experimental specimens. The equivalent viscous damping coefficient characterizes the energy dissipation performance of specimens at different loading stages; the cumulative energy consumption characterizes the overall energy dissipation capacity of specimens during the whole loading process.

As shown in Figure 11, the area of each hysteresis loop in the hysteresis curve represents the energy-consuming capacity of the specimens under this cycle. When other conditions are the same, the larger the area of the hysteresis loop, the better the energy consumption capability of the specimen. The equivalent viscous damping coefficient  $h_e$  of specimens is calculated as

$$h_e = \frac{1}{2\pi} \times \frac{S_{ABC} + S_{CDA}}{S_{ODG} + S_{OBH}}. \quad (2)$$

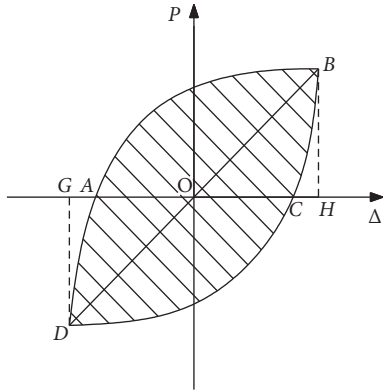


FIGURE 11:  $P$ - $\Delta$  hysteretic curve, representing the energy-consuming capacity of the specimen.

As shown in Figure 12, the equivalent viscous damping coefficient ( $h_e$ ) of the specimen and the displacement ( $\Delta$ ) curve of the column end were calculated for each specimen. At the initial stage of loading, the energy consumption of the specimen increased as the loading displacement increased. When the specimen was cracked, stress redistribution occurred inside the specimen, thereby impacting the stress and deformation of the specimen and decreasing the energy consumption. As the loading displacement continued to increase, the crack continued opening and closing, thus increasing the energy consumption of the specimen. When the specimen yielded, the internal longitudinal reinforcement of the specimen yielded, and the stress redistribution occurred again inside the specimen, thus decreasing the energy consumption of the specimen. With continuous loading, cracks of the specimen kept opening and closing, and energy consumption continued increasing until the specimen was destroyed. The equivalent viscous damping coefficient of each specimen increased as a whole, which indicated that the damage of the specimen increased as the horizontal deformation increased during the loading process, thereby increasing the energy consumption of the specimen (Figure 12).

Cumulative energy consumption refers to the sum of all hysteresis loop areas generated from the beginning of the load application to the ultimate displacement point. The larger the value, the stronger the energy dissipation capacity of the specimen and the better the seismic performance. As shown in Table 6, the cumulative energy dissipation was calculated for each specimen.

In contrast to SC-1, the cumulative energy consumption of SC-2 increased by 37%, indicating that the oblique horizontal loading led to more serious cumulative damage and the consumption of more energy. Compared to SC-2, the accumulated energy consumption value of SC-3 decreased by approximately 16%, possibly due to the premature failure of specimen and the increase of the axial pressure ratio, which reduces the cumulative energy consumption capacity of specimen. In contrast to specimen SC-3, the cumulative energy consumption values of specimens SC-4, SC-5, and SC-6 all improved, with increase rates of 222%, 278%, and 412%, respectively. This is because high-

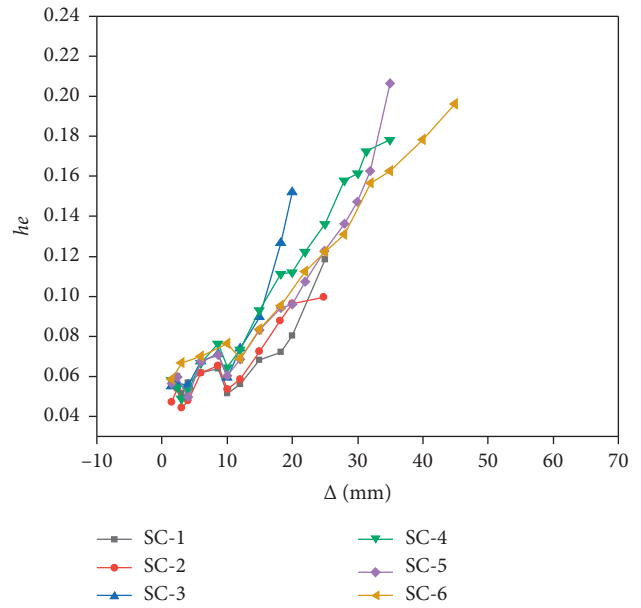


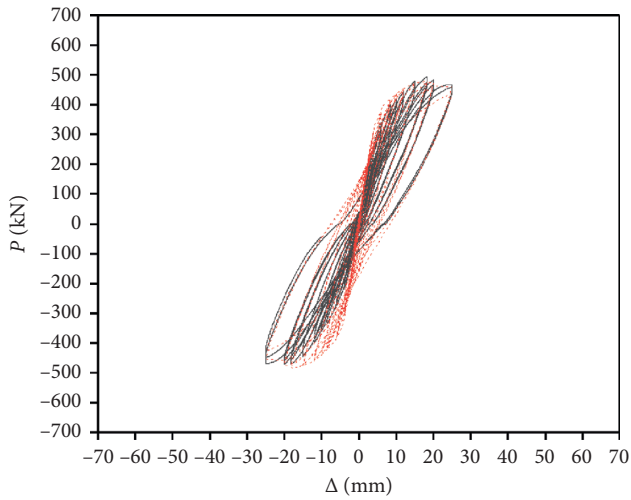
FIGURE 12: Viscous damping coefficient curves of each specimen. The equivalent viscous damping coefficient ( $h_e$ ) of the specimen and the displacement ( $\Delta$ ) curve of the column end were calculated for each specimen.

TABLE 6: Accumulated dissipated energy ( $E_p$ ) of all specimens.

Specimen	$E_p$ (kN·mm)	Relative value
SC-1	49770	1
SC-2	68307	1.37
SC-3	41784	0.84
SC-4	160490	3.22
SC-5	187933	3.78
SC-6	254794	5.12

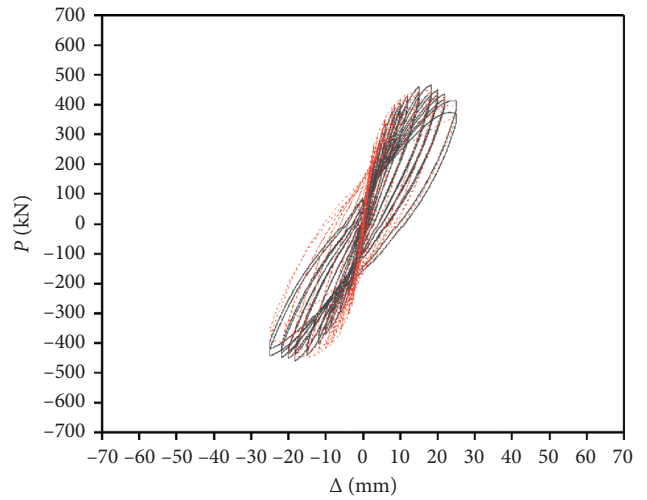
strength stirrups with small spacing, wound CFRP at the end of the column, and steel plate mesh at the end of the column limit the shedding of concrete and thus increase the work of the concrete.

**3.7. OpenSees Finite Element Simulation.** The open-source finite element program OpenSees (Open System for Earthquake Engineering Simulation) was used as a platform to numerically simulate the experimental specimens. The model used displacement-based nonlinear beam-column elements. Three nodes along the height of the column were used to form two units, wherein the top node was free end and the bottom node was embedded. The P-Delta effect caused by the vertical load was considered by the P-DeltaCrdTransf command. The fiber model was used to define the relationship of the cross section restoring force at the unit integration point. The longitudinal reinforcement was modeled using the Reinforcing Steel uniaxial material provided in OpenSees which was based on the Chang-Mander uniaxial material model [21] and simulated the isotropic hardening behavior of steel bars. The concrete was simulated by Concrete 02 provided by OpenSees. The material was based on the Kent-Scott-Park uniaxial material



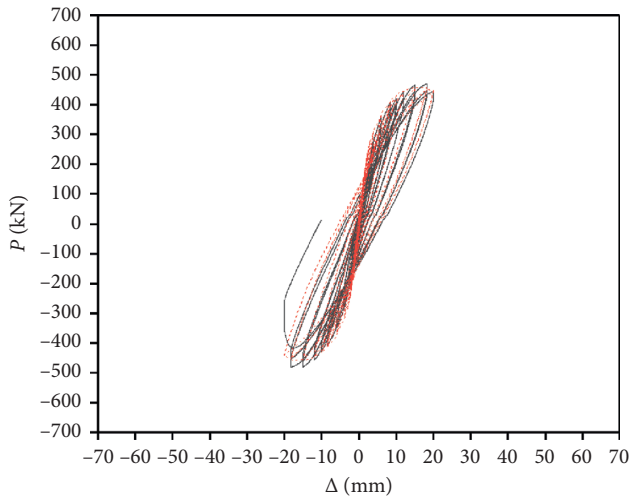
— Black = experimentally derived  
 - - - Red = finite element

(a)



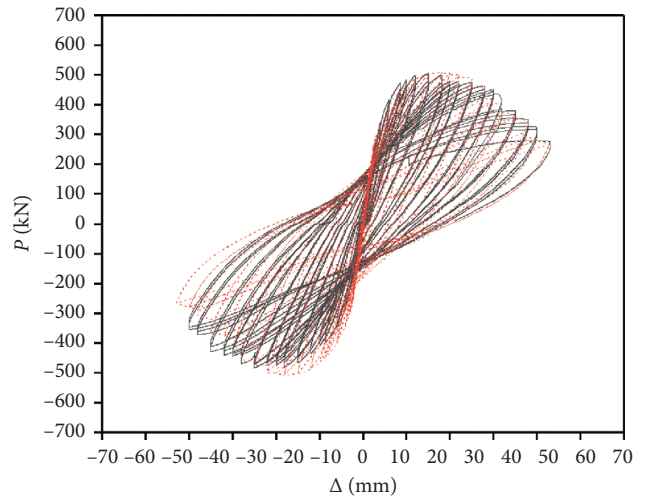
— Black = experimentally derived  
 - - - Red = finite element

(b)



— Black = experimentally derived  
 - - - Red = finite element

(c)



— Black = experimentally derived  
 - - - Red = finite element

(d)

FIGURE 13: Continued.

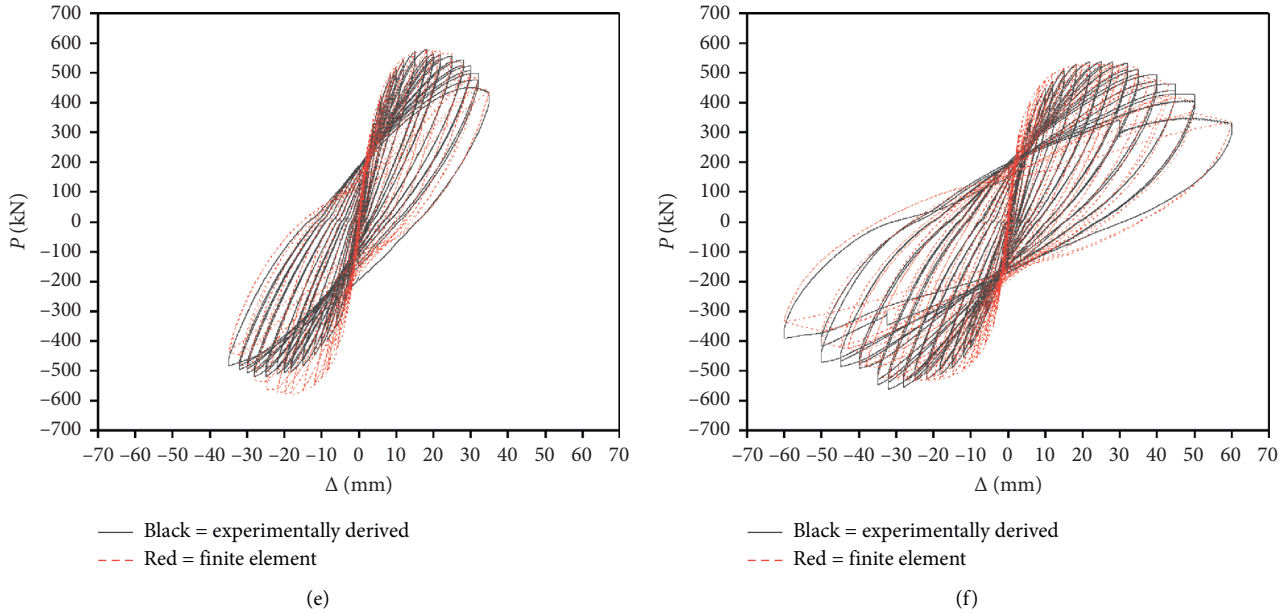


FIGURE 13: OpenSees finite element simulations compared with the experimentally derived hysteresis curve for each specimen. Results comparison of (a) SC-1, (b) SC-2, (c) SC-3, (d) SC-4, (e) SC-5, and (f) SC-6.

model [22]. The model included the tensile mechanical properties of the concrete, the stiffness degradation, and the energy dissipation behavior of the concrete during reciprocating loading. For the concrete in the core area, the Mander model [23,24] was used to consider the restraining effect of stirrups on concrete. Here, the stress-strain relationship of CFRP-constrained concrete was established using the Concrete 02 material. The stress and strain at the peak point were the same as the peak-point stress and strain of the concrete bound by the stirrup. The stress and strain at the limit point were calculated using the peak-point stress and strain of the Lam-Teng model [25,26]. There was little research on concrete columns reinforced by steel plate mesh and no specific theoretical models. Based on the existing steel mesh reinforced concrete column, the Concrete 02 material in this study was used to establish the stress-strain relationship of the steel plate mesh to the concrete; equations (3) and (4) were used to calculate the peak concrete stress  $f_{cc}$  after confinement [19]. The peak strain was 4 times that of the peak stress of unconstrained concrete; the limit point stress was twice that of the ultimate stress of unconstrained concrete; the calculations of the remaining characteristic parameters were consistent with the calculation results of the unconstrained concrete:

$$f_{cc} = (1 + 0.77\lambda_v)f_{ck}, \quad (3)$$

$$\lambda_v = \frac{\rho_v f_{yv}}{f_{ck}}, \quad (4)$$

where  $f_{ck}$  is the axial compressive strength of the concrete,  $\lambda_v$  is the eigenvalue of the stirrup,  $f_{yv}$  is the yield strength of the steel plate mesh, and  $\rho_v$  is the volumetric ratio of the steel plate mesh.

The vertical load was applied incrementally in 10 steps using the gravity loading module provided by OpenSees and

was held constant after the vertical load was completed. The horizontal load was applied in time series, and the loading system was consistent with the experimental procedures used in this study.

The hysteresis curves for SC-1 through SC-6 generated by the OpenSees finite element analysis were compared to the experimentally generated hysteresis curves, as shown in Figure 13. The curves generated by OpenSees are in good agreement with the experimental results.

#### 4. Conclusion

Here, six short concrete columns with high-strength longitudinal reinforcements were subjected to low-cycle repeated loading tests. By comparing and analyzing the test results based on observed test phenomena, the following conclusions are drawn:

- (1) Compared to the horizontally loaded test specimens, the strength of the diagonally loaded specimens decreased and the stiffness degradation trend accelerated; this indicates that the effect of oblique loading is unfavorable to the strength and stiffness of the specimens.
- (2) Under the action of oblique load, as the axial compression ratio increases, the strength of the specimen increases; however, the deformation capacity becomes worse, the stiffness becomes severely degraded, and the specimen is prone to shear brittle failure.
- (3) Under the action of oblique load, the reinforcement measures of the CFRP at the end of the column improve the strength and energy consumption of the specimen; however, the higher axial compression

ratio makes the CFRP more prone to damage and does not improve the deformation performance of the specimen. However, the local reinforcement measures of the steel plate mesh on the end of the column not only increase the strength and energy consumption of the specimen but also improve the deformation ability of the specimen and the seismic performance of the specimen.

- (4) In contrast to the unreinforced specimens, the addition of the high-strength stirrups with small spacing, column-end wound CFRP, and column-end outer steel plate mesh all improve the strength, deformation capacity, and energy consumption capacity of the specimens. The addition of the high-strength stirrups with small spacing and the column-end outer steel plate mesh both altered the failure mode of the specimen, transforming it from shear failure to bending shear failure. This shows that the above measures can effectively improve the seismic performance of the test specimen under the action of oblique loads with a high axial compression ratio.
- (5) Under the action of a high axial pressure ratio oblique load, by selecting the appropriate fiber unit and material constitutive relationship, the OpenSees program can obtain a simulation result that is in good agreement with the test hysteresis curve. This verifies the validity of the numerical simulation and provides a certain basis for subsequent and extended numerical simulation analyses.

## Data Availability

All data or models used to support the findings of this study are included within the article. Some data or models that support the findings of this study are available from the corresponding author upon reasonable request.

## Conflicts of Interest

The authors declare that there are no conflicts of interest regarding the publication of this paper.

## Acknowledgments

This work was supported by the Natural Science Foundation of Shandong Province under Grant nos. ZR2015EQ017 and ZR2018MEE044 and Off-Campus Development Project of Key Laboratory of Beijing University of Technology under Grant no. 2020B03. The authors are grateful to the Key Laboratory of Building Structural Retrofitting and Underground Space Engineering (Shandong Jianzhu University), Ministry of Education, for accommodating the use of the equipment and facilities, Professor Xingquan Zhao for providing computer equipment for numerical simulation of the experiment, and Editage (<http://www.editage.cn>) for English language editing.

## References

- [1] A. Ghobarah and K. Galal, "Seismic rehabilitation of short rectangular RC columns," *Journal of Earthquake Engineering*, vol. 8, no. 1, pp. 45–68, 2004.
- [2] Y. A. Li, T. Y. Huang, and S. J. Hwang, "Seismic response of reinforced concrete short columns failed in shear," *ACI Structural Journal*, vol. 111, no. 4, pp. 945–954, 2014.
- [3] H. Takizawa and H. Aoyama, "Biaxial effects in modelling earthquake response of R/C structures," *Earthquake Engineering & Structural Dynamics*, vol. 4, no. 6, pp. 523–552, 1976.
- [4] H. Umehara and J. O. Jirsa, "Short rectangular RC columns under bidirectional loadings," *Journal of Structural Engineering*, vol. 110, no. 3, pp. 605–618, 1984.
- [5] K. A. Woodward and J. O. Jirsa, "Influence of reinforcement on RC short column lateral resistance," *Journal of Structural Engineering*, vol. 110, no. 1, pp. 90–104, 1984.
- [6] K. Maruyama, H. Ramirez, and J. O. Jirsa, "Short RC columns under bilateral load histories," *Journal of Structural Engineering*, vol. 110, no. 1, pp. 120–137, 1984.
- [7] H. Rodrigues, H. Varum, A. Arêde, and A. G. Costa, "Behaviour of reinforced concrete column under biaxial cyclic loading—state of the art," *International Journal of Advanced Structural Engineering*, vol. 5, no. 1, pp. 1–12, 2013.
- [8] D. Wang, L. Huang, T. Yu, and Z. Wang, "Seismic performance of CFRP-retrofitted large-scale square RC columns with high axial compression ratios," *Journal of Composites for Construction*, vol. 21, no. 5, Article ID 04017031, 2017.
- [9] J. Yang and J. Wang, "Seismic performance of shear-controlled CFRP-strengthened high-strength concrete square columns under simulated seismic load," *Journal of Composites for Construction*, vol. 22, no. 6, Article ID 04018061, 2018.
- [10] X. Zhou and J. Liu, "Seismic behavior and shear strength of tubed RC short columns," *Journal of Constructional Steel Research*, vol. 66, no. 3, pp. 385–397, 2010.
- [11] H. Ma, J. Xue, Y. Liu, and X. Zhang, "Cyclic loading tests and shear strength of steel reinforced recycled concrete short columns," *Engineering Structures*, vol. 92, pp. 55–68, 2015.
- [12] D. Sokoli and W. M. Ghannoum, "High-strength reinforcement in columns under high shear stresses," *ACI Structural Journal*, vol. 113, no. 3, pp. 605–614, 2016.
- [13] H. Ding, Y. Liu, C. Han, and Y. Guo, "Seismic performance of high-strength short concrete column with high-strength stirrups constraints," *Transactions of Tianjin University*, vol. 23, no. 4, pp. 360–369, 2017.
- [14] H. O. Shin, Y. S. Yoon, W. D. Cook, and D. Mitchell, "Axial load response of ultra-high-strength concrete columns and high-strength reinforcement," *Transactions of Tianjin University*, vol. 113, no. 2, pp. 325–336, 216.
- [15] L. A. E. Shehata, M. L. A. V. Carneiro, and L. C. D. Shehata, "Strength of short concrete columns confined with CFRP sheets," *Materials and Structures*, vol. 35, pp. 50–58, 2002.
- [16] F. Colomb, H. Tobbi, E. Ferrier, and P. Hamelin, "Seismic retrofit of reinforced concrete short columns by CFRP materials fit of reinforced concrete short columns by CFRP materials," *Composite Structures*, vol. 82, no. 4, pp. 475–487, 2008.
- [17] K. Galal, A. Arafa, and A. Ghobarah, "Retrofit of RC square short columns," *Engineering Structures*, vol. 27, no. 5, pp. 801–813, 2005.
- [18] R. Morshed and M. T. Kazemi, "Seismic shear strengthening of R/C beams and columns with expanded steel meshes,"

- Structural Engineering and Mechanics*, vol. 21, no. 3, pp. 333–350, 2005.
- [19] Z. Li, X. Wang, Y. Xie, and C. Yu, “Experimental study of seismic behavior of high-strength concrete columns with expanded metal lath,” *Journal of North China University of Science and Technology (Natural Science Edition)*, China, vol. 40, no. 4, pp. 51–58, 2018.
- [20] Z. Li, C. Yu, Y. Xie, H. Ma, and Z. Tang, “Size effect on seismic performance of high-strength reinforced concrete columns subjected to monotonic and cyclic loading,” *Engineering Structures*, vol. 183, no. 15, pp. 206–219, 2019.
- [21] S. K. Kunnath, Y. Heo, and J. F. Mohle, “Nonlinear uniaxial material model for reinforcing steel bars,” *Journal of Structural Engineering*, vol. 135, no. 4, pp. 335–343, 2009.
- [22] B. D. Scott, R. Park, and M. J. N. Priestley, “Stress-strain behavior of concrete confined by overlapping hoops at low and high strain rates,” *ACI Journal*, vol. 79, no. 1, pp. 13–27, 1982.
- [23] J. B. Mander, M. J. N. Priestley, and R. Park, “Theoretical stress-strain model for confined concrete,” *Journal of Structural Engineering*, vol. 114, no. 8, pp. 1804–1826, 1988.
- [24] J. B. Mander, M. J. N. Priestley, and R. Park, “Observed stress-strain behavior of confined concrete,” *Journal of Structural Engineering*, vol. 114, no. 8, pp. 1827–1849, 1988.
- [25] L. Lam and J. Teng, “Design-oriented stress-strain model for FRP-confined concrete,” *Construction and Building Materials*, vol. 17, no. 7, pp. 471–489, 2003.
- [26] L. Lam and J. G. Teng, “Design-Oriented stress-strain model for FRP-confined concrete in rectangular columns,” *Journal of Reinforced Plastics and Composites*, vol. 22, no. 13, pp. 1149–1186, 2003.